ELSEVIER

Contents lists available at ScienceDirect

Tribology International

journal homepage: www.elsevier.com/locate/triboint



Check for updates

Arc erosion and degradation analysis of carbon nanotube-reinforced silver and copper composites for DC switches

Bruno Alderete ^{a,*} , Francisco A. Delfin ^{b,c}, Frank Mücklich ^a, Sebastian Suarez ^a

- a Chair of Functional Materials, Department of Materials Science and Engineering, Saarland University, Campus D3.3, Saarbrücken 66123, Germany
- ^b Department of Materials Science, University of Applied Sciences Upper Austria, Stelzhamerstraße 23, Wels 4600, Austria
- c Universidad Tecnológica Nacional, Facultad Regional Concepción del Uruguay, Ing. Pereyra 676, Concepción del Uruguay, Entre Ríos E3264BTD, Argentina

ARTICLE INFO

Keywords: Carbon nanotubes Arc erosion Metal matrix composites Switching electrical contacts

ABSTRACT

Hot switching creates an electrical arc that erodes electrodes through ion and electron bombardment. This study characterizes arc erosion craters from a single-break operation of carbon nanotube (CNT)-reinforced composite and reference materials. Crater morphology was analyzed via confocal laser and electron microscopy, in addition to energy dispersive X-ray and Raman spectroscopy. Composites of up to 2 wt% resulted in crater roughness, displaced volume, and crater dimensions similar to reference materials. Higher CNT concentrations led to increased roughness and material displacement. Although CNT did not affect the molten front's dimensions, it reduced molten pool duration. Raman spectroscopy confirmed CNT structural integrity post-manufacturing, despite minor degradation. CNT-reinforced silver and copper composites (up to 2 wt%) demonstrate potential for cost-effective, durable switching electrodes.

1. Introduction

A switching device is an electrical component that is responsible for interrupting the flow of current in a circuit. The necessity for current interruption may be attributed to the specific characteristics of the application in question, such as the use of electromechanical relays and contactors. Alternatively, it may be a consequence of safety considerations, as exemplified by the deployment of magnetic circuit breakers and ground fault interrupters. During an electrically loaded break operation (known as hot switching), the separation of the electrodes results in an increase in the current density flowing through the contacting asperities (also known as a-spots) [1]. The elevated current density results in the generation of localized heat at the asperities. As the real contact area tends to zero and the constriction resistance increases, the temperature at the asperities exceed the melting point of the contacting metals. The molten material is drawn by the receding electrode, thereby generating a molten bridge between the two electrodes. As the gap between the electrodes increases, the bridge is further extended, thereby further increasing the current density. The molten bridge is extended until it becomes unstable and ruptures [1]. Instability arises either from the introduction of cooler material at the base of the bridge or from the ejection of particles caused by temperatures surpassing the metal's boiling point [1]. Upon the rupture of the bridge, the arc is established, resulting in the release of metallic vapor into the gap between the electrodes. The release of metallic vapor into the gap significantly increases the pressure. However, as the vapor expands into the surrounding low-pressure regions, a pseudo-arc is ignited in which the current is conducted by the ions. Under atmospheric conditions, the movement of gases into the inter-electrode gap is driven by a decrease in pressure. This influx of gases subsequently leads to the transition of the arc from a metallic phase (where ions are the primary current carriers) into a gaseous phase (where electrons are the primary current carriers)

In the early stages of the arc, the anode is eroded on account of electron bombardment, while the cathode gains mass as particles condense and recombine on its surface. This leads to a transfer of material from the anode towards the cathode [2]. For arcs with longer durations, a transition phase occurs, during which ion bombardment causes the cathode to lose mass [3]. This transition is dictated by both the arc's length and duration. The former determines if this transition takes place, whereas the latter is the dominant factor influencing the direction of mass transfer [4]. During the shift from anodic to cathodic arc, the material previously deposited on the cathode is removed, thus leading to net zero erosion [5]. The point of net zero erosion is

E-mail address: bruno.alderete@uni-saarland.de (B. Alderete).

^{*} Corresponding author.

determined by the amount of material transferred during anodic erosion. In other words, how much material needs to be eroded from the cathode to completely sputter material that was transferred from the anode. This is influenced both by the arc's duration and the electrode's composition [4]. The duration of the arc depends on the type of arc that is ignited, which is in turn determined by the electrical load - i.e., resistive, capacitive, inductive. Whereas the material selection determines the erosion rate of the electrodes. A longer anode loss phase (and consequently a longer cathode gain phase) and materials that erode more easily, will lead to more material being transferred towards the cathode, thus prolonging net zero erosion. Nevertheless, the anodic to cathodic arc transition is unaffected by electrode material and arc duration; it is only dependent on arc length. The current levels flowing through the electrodes prior to breaking do not affect the type of arc that ignites. However, the current does amplify the arc's energy, which can significantly affect erosion (and postpone net zero erosion [5]). Breaking at elevated currents leads to higher material removal rates and larger sized craters. Therefore, high currents and longer arc durations tend to produce much rougher craters [6,7].

The service life of a circuit breaker depends upon its capacity to withstand erosion due to arcing. In order to ensure optimal performance and safety, electrode materials should exhibit a low electrical resistance, be resistant to excessive heating, be erosion-resistant, demonstrate good interruption capabilities, not be toxic, be cost-effective, exhibit low welding tendencies, and low weld force to ensure that the circuit opens when required [1,8]. Silver is a material that is extensively utilized in switching applications, presenting exceptional conductivity and low welding potential. The performance and durability of silver electrodes can be further enhanced by alloying it with zinc, nickel, copper, tungsten, palladium, among other metals, or by using silver-metal oxide composite materials, including silver-cadmium oxide, silver-zinc oxide, silver-tungsten oxide, silver-tin oxide, and others [1,3,8-11]. Additionally, copper is used in certain switching applications for its excellent conductivity and relatively low cost (particularly when compared to silver). However, copper has a higher welding potential than silver. Therefore, to improve weld resistance, copper electrodes are often coated with silver-based materials. Additional techniques employed to enhance the switching performance of copper include the deposition of tin coatings or alloying copper with elements such as zinc, tin, cadmium, chromium, or tellurium [1,8].

Previous researchers have evaluated the switching behavior of graphite-based silver and copper electrodes [12-17]. The studies underscore the enhanced switching performance by reducing the weldability of the electrodes even when subjected to elevated switching currents [8,18]. The studies also demonstrate how the formation of non-conductive oxide layers on the electrode's surface is prevented, thus ensuring low resistances [17]. However, the performance of graphite-containing metal matrix composite (MMC) electrodes is influenced by graphite's relative position within the composite due to its anisotropic nature. Additionally, incorporating graphite into these metals tends to decrease electrical conductivity, as well as increasing erosion rates and the likelihood of arc re-ignition [17,19]. Nevertheless, graphite-based copper composite materials find applications when friction and (high current) arc discharges act simultaneously in the system [20-22]. Moreover, research on copper-tungsten composite electrodes has shown that the addition of graphene can improve the electrodes' hardness and conductivity [23]. As is the case with graphite, the addition of graphene increases erosion rates. Nonetheless, graphene promotes the dispersion of the arc while also increasing the viscosity of the molten pool. Likewise, copper-tungsten composites using copper doped with reduced graphene oxide have proven to increase molten pool viscosity while also reducing solidification times; thus inhibiting fast flow and splashing of the molten pool [24]. Furthermore, studies on the high current performance of carbon-based copper composite have shown that increasing the contact load between the electrodes can also aid in hindering arc discharges [25]. Moreover, carbon-reinforced

silver-based composite materials have shown improved mechanical properties, while also reducing weldability and material transfer during arcing [26,27].

Our previous research has examined and reported on the characteristics of the arc generated, electrical contact resistance, reinforcement phase distribution, and the impact of carbon nanotube (CNT) concentration on arc behavior [28]; highlighting the promising performance of the proposed composites. Moreover, the addition of CNT as a reinforcement phase promotes contact repeatability due to their elasticity, as well as improved electrical, fatigue, and tribological performance [29-32]. Like graphite, CNT also present anisotropy in their transport properties. However, CNT have a great tendency to form agglomerates due to van der Waals interactions. Large CNT bundles are - in part broken down during the manufacturing of the MMC in order to take advantage of the exceptional properties that these nanostructures possess [33,34]. However, during this step, it is crucial that the CNT do not sustain excessive amounts of damage which could lead to structural degradation [35]. Consequently, the reinforcement phase in the MMC still consists of CNT clusters (although considerably smaller). While CNT agglomerates are often regarded as detrimental, due to the weakening of their intrinsic properties, in this context they can be advantageous. Specifically, agglomerates of multi-walled CNT help mitigate the anisotropic transport properties of individual nanotubes, as they statistically include at least one tube exhibiting metallic conductivity [36].

It is therefore the aim of this study to evaluate the degradation of CNT-reinforced silver and copper MMC and assess their potential as switching electrodes in low-voltage direct current circuits. Switching devices make-and-break the circuit numerous times, which will undoubtedly affect the erosion rate of the electrodes. However, the fundamental interactions between the contacting electrodes remain the same irrespective of the number of times that the circuit is interrupted. Accordingly, this work focuses on characterizing the crater resulting from a single break operation. This consideration provides insight and enables the assessment of the initial performance of the proposed MMC, particularly in comparison with reference and standard switching materials.

The arc erosion craters produced were micrographed via confocal laser scanning microscopy (CLSM) and scanning electron microscopy (SEM), whereas chemical analysis was carried out via energy dispersive X-ray spectroscopy (EDS). The area affected beneath the arc erosion crater was visualized by conducting focused ion beam (FIB) cross sections at the center of the craters. The CLSM measurements were employed to determine the most relevant crater attributes - i.e., dimensions, topographic parameters, displaced material volume, and load-bearing capacity following the initial opening cycle. Finite element method thermal simulations were conducted on the pure metals and CNT-reinforced MMC based on the real power input of the electrical arcs. Through this methodology, maximum temperatures, dimensions of the melting and boiling fronts, duration of the molten pool, and evaporation times were determined. Furthermore, Raman spectroscopy was carried out to assess the structural integrity of the CNT clusters within and outside the crater to determine the extent of damage that the reinforcement phase may have sustained during arcing.

2. Materials and methods

2.1. Materials

CNT-reinforced silver and copper metal matrix composites were fabricated using powder metallurgy with CNT concentrations of 1, 2, and 3 wt%. The metallic matrices consisted of silver flakes and dendritic copper powders. The silver flakes (Alfa Aesar GmbH) have a purity of 99.9 % and a particle size distribution where at least 80 % of the flakes were below 20 μm . The dendritic copper powder (Alfa Aesar GmbH) used has a 325-mesh size and 99 % purity. The multi-walled CNT were synthesized via chemical vapor deposition (Graphene Supermarket).

The reinforcement phase possesses an outer diameter ranging from 50 to 85 nm, a length of 10– $15\,\mu m$ in their as-received state, and a carbon purity exceeding 94 %.

To comprehensively evaluate the feasibility of the proposed MMC, their performance was compared to that of pure metals and commonly used switching materials. High purity silver (99.95 %, Alfa Aesar GmbH) and copper (99.9 %, Goodfellows Cambridge Limited) rods served as pure metal benchmarks. Furthermore, unreinforced (0 wt%) sintered silver and copper reference samples were manufactured using the same metallic powders as the reinforced samples. Additionally, silver-based switching materials were assessed due to their extensive commercial applications; namely Ag/Ni 90/10, Ag/SnO₂ 88/12, Ag/SnO₂ 90/10, and Ag/SnO₂ 92/8 (Umicore N.V.).

In all arc erosion tests, hard gold-coated (AuCo_{0.2}) silver-nickel core (AgNi_{0.15}) rivets (Adam Bornbaum GmbH, Germany) were employed as counter electrodes. The rivets featured a hemispherical geometry (4 mm radius of curvature), a hardness of 1.38 ± 0.01 GPa (determined via Vickers hardness testing), and an S_q of $0.3~\mu m$. While it is usual that both electrodes are composed of the same material, hard gold counter electrodes were chosen in this work for several reasons: 1) using only one material as counter electrode ensures consistent and comparable results irrespective of the material being tested; 2) hard gold counter electrodes guarantee similar oxidative state throughout the experiments; 3) the higher hardness of the counter electrodes ensures that plastic deformation occurs predominantly on the materials in question; 4) hard gold counter electrodes have similar melting point as the materials herein studied [8]; and 5) gold can be used as a "trace" material to observe how and in which direction material transfer took place during arcing.

2.2. MMC manufacturing

The CNT were dispersed in ethylene glycol through a combination of homogenization (Ultra-Turrax T25, IKA) and ultrasonication. The metallic powder was then introduced into the colloid, followed by an additional homogenization step. The solvent was subsequently evaporated in a ventilated furnace at 150 $^{\circ}\mathrm{C}$ for at least 24 h. After solvent removal, green pellets with an 8 mm diameter were formed by placing the CNT-metallic powder mixture into a steel die and applying a pressure of 990 MPa for approximately 30 s.

To achieve further densification, ensuring a relative density of at least 95 %, the green pellets underwent hot uniaxial pressing. To minimize the likelihood of sample oxidation, this densification step was conducted under vacuum (2×10^{-6} mbar). Both silver and copper samples were sintered at a pressure of 264 MPa and a temperature of 750 °C. The isothermal holding time was 7.5 h for silver samples and 2.5 h for copper samples. Additional details on colloidal mixing and MMC sample fabrication can be found in [29,30].

2.3. Arc erosion tests

The arc was induced by simulating a break operation between the MMC or reference material and the hard gold counter electrode. Both electrodes were secured onto a customized electrical testing rig [37]. The samples were positioned on a movable stage and connected to the positive terminal (anode) of a 3000 W direct current power source (Gossen Metrawatt SSP 3000-52). The counter electrode, on the other hand, was mounted onto the fixed stage of the testing rig and connected to the negative terminal (cathode) of the power source. Voltage drops before, during, and after the break operation were recorded using an oscilloscope (LeCroy WaveRunner 6100 A). The current was stored using the same device and measured with a LeCroy CP031 current probe [38]. Four 50 W automotive halogen lamps served as a pure ohmic load, totaling 200 W. A constant voltage of $13.5\,\mathrm{V}$ was used throughout the arc erosion tests, resulting in an approximate current of 17 A (further details can be found in [28]). A standard normal load of 4 N was applied between the electrodes, with a 10 s stabilization time allowed before

opening the circuit to ensure a steady-state current during breaking. Once the current had stabilized, the linear stage retracted with a constant acceleration of 8000 mm/s², reaching a peak speed of 58 mm/s. Further details on the setup's precision and schematic representations were previously provided by Puyol et al. and Suarez et al. [37,38]. A minimum of three switching operations were performed per sample type, each at a different spot. Although the reinforcement phase is not homogeneously distributed, arc erosion tests on samples with identical CNT concentrations did not show significant variations - see [28]. Between each measurement, the current probe was degaussed, and a new rivet was mounted on the testing rig. The rivets were cleaned with an isopropanol-based contact cleaner and dried using compressed air before each test. All experiments were conducted under atmospheric conditions – 23 ± 1 $^{\circ}\text{C}$ and $23\pm2\,\%$ relative humidity. Prior to arc erosion testing, all samples were mirror polished, achieving roughness values ranging from 0.3 to 0.6 µm. The root mean square roughness of each electrode prior to arc erosion tests are shown in Supplementary Table 1.

2.4. Confocal laser and scanning electron microscopy

The samples and rivets were micrographed via confocal laser scanning microscopy (LEXT OLS4100, Olympus) using a laser wavelength of 532 nm. Micrographs of the arc erosion craters on the samples' surface were acquired with a magnification of $50\times$, whereas $20\times$ magnification was used for the counter electrodes due to their curvature. At least three arc erosion craters were micrographed per sample. Morphological and topographic analysis of the arc erosion craters conducted via CLSM were carried out applying a mask to highlight the region of interest. Therefore, the influence of the unaffected regions surrounding the craters were eliminated.

SEM micrographs of the arc erosion craters on the samples were acquired using an ICE detector and an acceleration voltage and beam current of 10 kV and 1.6 nA, respectively (Thermo-Fisher Helios $^{\rm TM}$ G4 PFIB CXe DualBeam $^{\rm TM}$ FIB/SEM equipped with an EDS detector EDAX Octane Elite Super). Furthermore, for a two-dimensional chemical distribution analysis, EDS mappings were acquired using 10 kV. FIB milling was carried out using Xe ions with an acceleration voltage of 30 kV and a beam current of 1 μ A. Subsequent ion polishing of the cross section was conducted using a beam current of 0.2 μ A, 60 nA, and 15 nA to minimize curtaining. An approximate volume of 0.5 mm was removed. The cross section was micrographed using an ICE and TLD detector, with an acceleration voltage and beam current of 5 kV and 1.6 nA, respectively.

2.5. Thermal simulations

Finite element method thermal simulations based on Fourier's law of heat conduction were carried out for each MMC and pure metal references using Flex-PDE software [39]. Effects of convection and radiation were neglected since these transfer modes are considered energy losses. In other words, convection and radiation are fractions of the arc's energy that are not absorbed by the electrode. Convection transfers a part of the arc's energy to the surrounding gas, while another part is lost through radiation. Moreover, the exact amount of heat that is transferred via these mechanisms differs significantly, depending on the literature [40-43]. In addition, the time frame in which the discharge occurs and the interaction time (in the µs range [28]) renders both convection and radiation marginal. Therefore, to simplify the simulations and to simulate the worst-case scenario, the thermal simulations were carried out under the assumption that 100 % of the arc's energy is absorbed by the electrode. The heat input was obtained by linearly fitting the power curves of each arc erosion test reported in [28]. The energy from the electrical arc was assumed to be cylindrical, with a radius of $50\,\mu m$, encountering a 1 mm in radius and height cylindrical electrode from the z-axis. All phase transitions were considered in the simulations by incorporating the power per unit of volume involved in solid-liquid and

Table 1Average crater attributes after a single break operation.

Sample	Crater area ($\times 10^4$) / μm^2	Crater surface area ($\times 10^4$) / μm^2	S-ratio	
Ag/Ni 90/10	3.03 ± 0.48	$\textbf{4.48} \pm \textbf{0.77}$	1.48 ± 0.03	
Ag/SnO ₂ 92/8	2.30 ± 0.16	3.21 ± 0.32	1.39 ± 0.05	
Ag/SnO ₂ 90/10	2.54 ± 0.29	3.47 ± 0.50	1.36 ± 0.05	
Ag/SnO ₂ 88/12	2.30 ± 0.33	3.14 ± 0.38	1.37 ± 0.03	
Ag rod	3.24 ± 0.25	$\textbf{4.81} \pm \textbf{0.44}$	1.43 ± 0.04	
Ag 0 %	3.21 ± 0.31	$\textbf{4.73} \pm \textbf{0.42}$	1.47 ± 0.02	
Ag 1 %	2.97 ± 0.44	5.18 ± 0.72	1.75 ± 0.02	
Ag 2 %	$\pmb{2.85 \pm 0.42}$	$\textbf{5.22} \pm \textbf{0.80}$	1.83 ± 0.04	
Ag 3 %	3.57 ± 0.73	$\textbf{7.64} \pm \textbf{2.77}$	2.07 ± 0.34	
Cu rod	2.08 ± 0.32	2.61 ± 0.35	1.26 ± 0.04	
Cu 0 %	2.72 ± 0.25	3.51 ± 0.30	1.29 ± 0.01	
Cu 1 %	2.41 ± 0.08	3.95 ± 0.13	1.64 ± 0.01	
Cu 2 %	2.33 ± 0.39	$\textbf{4.06} \pm \textbf{0.66}$	1.74 ± 0.02	
Cu 3 %	$\pmb{2.77 \pm 0.45}$	$\textbf{5.27} \pm \textbf{0.76}$	1.91 ± 0.03	

Table 2Average volume above and below the datum line for arc erosion craters in reference and MMC samples.

Sample	Volume above (×10 ⁴) /μm ³	Volume below ($\times 10^4$) / μ m ³
Ag/Ni 90/10	$\boldsymbol{1.89 \pm 0.22}$	1.53 ± 0.22
Ag/SnO2 92/8	0.70 ± 0.09	1.68 ± 0.18
Ag/SnO ₂ 90/10	1.30 ± 0.19	1.44 ± 0.20
Ag/SnO ₂ 88/12	1.00 ± 0.11	1.73 ± 0.17
Ag rod	3.20 ± 0.10	1.80 ± 0.13
Ag 0 %	2.09 ± 0.18	1.57 ± 0.20
Ag 1 %	1.78 ± 0.21	1.97 ± 0.29
Ag 2 %	1.46 ± 0.27	2.21 ± 0.11
Ag 3 %	3.81 ± 1.11	3.17 ± 3.47
Cu rod	1.11 ± 0.11	1.19 ± 0.06
Cu 0 %	1.16 ± 0.18	1.42 ± 0.23
Cu 1 %	1.31 ± 0.13	2.73 ± 0.21
Cu 2%	1.37 ± 0.16	1.52 ± 0.04
Cu 3 %	3.60 ± 0.85	1.28 ± 0.54

liquid-vapor phase transitions, as described by Soldera et al. [43]. From the thermal simulations, the maximum electrode temperatures, dimensions of the molten and boiling fronts, and duration of material melting and evaporation were determined. The simulations were conducted under the assumption that evaporated material left the system – i.e., there is no re-deposition through condensation. Material properties (i.e., melting and boiling temperatures, specific heat capacity, thermal conductivity, and density) were obtained from [1,44–49]. Due to the aleatory nature of the reinforcement phase's distribution within the MMC, the specific heat capacity and thermal conductivity for the MMC were determined using the effective medium theory [50].

2.6. Raman spectroscopy

A Raman spectrometer (Horiba XploRA Plus) was used to evaluate the structural integrity of the reinforcement phase prior to and after arc erosion tests. The Raman spectrometer was equipped with a 532 nm laser. The data was acquired using a grating of 2400 lines mm⁻¹, a $100 \times$ objective, and a laser power of 2 mW, with a spectral resolution of approximately 5.9 cm⁻¹. The acquisition time was determined for every measurement using the auto-exposure tool, thus obtaining a better signal-to-noise ratio. Within the same measurement, at least three repetitions were performed to reduce sporadic external influences and to improve smoothness. Measurements were conducted on at least three different CNT clusters within and outside of the crater, thereby obtaining statistically significant results. Prior to analyzing the data, the spectra's cosmic ray and background were removed using CrystalSleuth [51], and the spectra intensities were normalized. The Raman peaks were subsequently fitted. The D- and G'-bands were fitted using a Lorentz fitting. The (G+D')-band was fitted using a combined Lorentz-Voigt fitting, whereas the G-band was fitted using a Lorentzian curve and the

D'-band a Voigtian curve [52]. Due to the convolution of these G- and D'-bands, the theoretical peak center values for graphite according to Ferrari and Robertson were fixed – i.e., $1582\,\mathrm{cm}^{-1}$ and $1620\,\mathrm{cm}^{-1}$ for the G- and D'-band, respectively [53]. Subsequently, the fitted Raman spectra were analyzed by determining the G-band's Raman shift (position of the peak's center), intensity and integral intensity ratios (i.e., the crystallinity and purity ratios: I_D/I_G , A_D/A_G , $I_{G'}/I_D$, and $A_{G'}/A_D$, respectively), and the FWHM of the G-band.

3. Results and discussions

3.1. Arc erosion crater morphology and topography

CLSM analysis of arc erosion craters provide insight into electrode erosion, material transfer, and topographical changes caused by the electrical arc. This technique was employed to obtain parameters such as crater dimensions, volumes of material displacement, and topographic parameters.

The average crater attributes determined via CLSM after a single break operation under a 200 W ohmic load for the reference and MMC samples are shown in Table 1. On average, the resulting crater area for the Ag/SnO $_2$ samples does not appear significantly affected by tin-oxide concentration. Irrespective of the reinforcement's concentrations, silver tin-oxide samples exhibit a crater area of approximately $2\times 10^4~\mu m^2.$ The silver-nickel sample, on the other hand, presents an average crater area of approximately $3\times 10^4~\mu m^2.$ The same trend is observed in the crater's surface area, and the corresponding S-ratio – i.e., the relationship between the crater's surface area (caused by topographic features) and the projected area of the crater.

For the silver MMC, the crater's attributes vary considerably depending on the sample type. The unreinforced silver samples (i.e., Ag rod and Ag 0%) and the Ag 3% sample exhibit the largest crater area. The arc erosion craters on the silver MMC with lower CNT concentrations (i.e., 1 and 2 wt%) exhibit a smaller projected area. Nevertheless, the surface area of these craters, and consequently the S-ratio, are larger than the unreinforced samples.

Among the silver samples, the craters on the unreinforced silver (Ag 0 %) have the smallest surface area. Contrarily, the craters on the reinforced silver samples exhibit an increasing surface area as the CNT concentrations increase. The same behavior can also be observed for the pure copper sample and CNT-reinforced copper MMC. Although the craters on the copper MMC are smaller than those on the silver MMC, the S-ratio values are similar.

The average volume above and below the datum line for the arc erosion crater were determined using CLSM, with the results being shown in Table 2. These results highlight the exceptional performance of the proposed materials. Apart from the 3 wt% samples, the reinforced samples perform similarly to the reference materials; although certain samples exhibit slight deviations compared to the references. These

minor deviations are due to the heterogeneous distribution of the reinforcement phase [28-30]. The heterogenous nature of the surfaces being contacted leads to minor changes in the features of the surface after arcing. This will depend on the contacting spot's characteristics - i.e., amount and size of CNT clusters at the contacting site. The 3 wt% samples not only show the largest craters in terms of area (see Table 1), but these samples also exhibit the largest volume displacement. The 3 wt % silver sample in particular presents the highest volume displacement values, both above and below the datum line. Although the Cu 3% sample also exhibits large volumes above the datum line, the volume below falls within the range of the other copper and reference samples. This suggests that the highest CNT concentrations herein considered favors rapid re-solidification and/or higher viscosity of the molten pool in Cu 3 %. The former is likely due to the improved thermal diffusivity of these MMC. Both these modifications increase the volume above the datum line and the crater's surface area by preventing – or reducing the time during which - the molten pool can flow and form a flat surface during cooling [23,24]. Silver MMC tend to present higher displaced volumes (above and below the datum line) than silver-based references and the copper MMC. This is a consequence of the lower viscosity of molten silver compared to that of copper and nickel [54]. Although silver and copper MMC exhibit larger displaced volumes than silver-nickel and silver-tin oxide references, the average volumes are not substantially greater – except for the 3 wt% MMC. Therefore, reinforcing silver and copper with 1-2 wt% CNT has minimal impact on material displacement (as well as crater area - Table 1), as evidenced by the similarity to their unreinforced counterparts.

Different roughness parameters of the craters were determined via CLSM, namely: the root mean square roughness S_q , the maximum valley depth S_v and peak height S_p , the maximum height S_z , and the skewness S_{sk} – shown in Table 3 [55]. S_v , S_p , S_z , and S_{sk} are particularly interesting since they provide further insight into the geometry of the resulting crater after the electrical arc, complementing the results from Table 1 and Table 2. The first three parameters express the overall height modification of the surface, whereas the latter represents the degree to which the asperities skew in reference to the datum line [55]. A positive S_{sk} value indicates that the surface presents few but very high peaks with many shallow valleys. A negative value, on the other hand, indicates the inverse scenario. An S_{sk} value that approaches zero implies a symmetrical distribution of peak heights and valley depths.

The topographic parameters presented in Table 3 showcase the surface modification endured by the electrodes after the break operation. The root mean square roughness shows that the arc on the silver samples results in the highest overall roughness. Nevertheless, the S_q values in the copper samples increase significantly faster as CNT concentrations increase. Comparing the unreinforced sintered samples (0 wt %) with the highest CNT concentration (3 wt%), the S_q in silver matrices increases by approximately 37.5 %. The S_q in the copper matrices, on the other hand, increases by over 69 %. If the 3 wt% samples are excluded,

due to the previous results shown in Table 1 and Table 2, the increase in roughness values is not as significant. Now, the silver samples only show a marginal 3% increase, whereas the copper samples' roughness increases by 40%. The increased roughness observed in samples with the highest CNT concentrations is caused by the rapid re-solidification and increased molten pool viscosity, as observed in Table 2.

The S_v , S_p and S_z roughness parameters show a similar trend as S_q . The Ag/Ni 90/10 sample shows the largest S_v , S_p and S_z values among the samples herein considered. Excluding this sample, again the 3 wt% samples exhibit the highest peaks and deepest valleys. Moreover, the S_{sk} parameter indicates that all samples exhibit skewed topographic features. In other words, the craters present numerous shallow peaks, with few high peaks. This is even the case in craters where the displaced volume above is greater than the volume displaced below the datum line (see Table 2). The pure sintered samples exhibiting a relatively symmetrical crater. Although most of the samples tend towards a positive topographic skew, the copper-based electrodes exhibit the lowest values. Thereby implying relatively symmetrical craters. This observation for the copper-based electrodes correlates with the values presented in Table 2, showing similar volumes displaced above and below the datum line

Table 4 Exemplary Abbott-Firestone parameters for reference, silver, and copper samples after a single break operation. Note that R_k , R_{pk} , and R_{yk} do not have a unit since these values were normalized in order to compare the values between different materials. Moreover, these exemplary values correspond to the arc erosion craters shown in the SEM micrographs (Fig. 1 and Supplementary Figure 5).

Sample	R_k	R_{pk}	$R_{\nu k}$	M_{r1} /%	M_{r2} /%
Ag/Ni 90/10	1.6	67.9	5.7	20.2	80.3
Ag/SnO ₂ 92/8	1.6	12.4	9.1	18.9	79.4
Ag/SnO ₂ 90/10	2.5	14.0	12.2	23.2	78.3
Ag/SnO ₂ 88/12	1.9	14.4	10.1	19.7	77.2
Ag rod	3.8	15.0	11.4	23.3	76.9
Ag 0 %	2.1	11.9	9.4	23.4	76.4
Ag 1 %	2.3	13.4	7.9	18.8	74.1
Ag 2 %	2.7	12.5	7.0	18.5	73.5
Ag 3 %*	6.5	11.3	9.3	24.1	82.5
Cu rod	0.9	12.4	8.0	15.1	79.3
Cu 0 %	2.0	10.4	11.4	24.6	81.9
Cu 1 %	2.2	14.5	10.3	20.5	76.6
Cu 2%	1.5	13.0	10.4	19.8	80.2
Cu 3 %*	6.9	15.8	10.6	19.8	80.0

* Although the values reported in this table correspond to the Abbott-Firestone parameters for a single arc erosion crater, multiple craters were characterized. The values presented herein are representative of each sample, with the variation between each crater not exceeding 20 % (except for the samples marked with an asterisk).

Table 3Average topographic parameters of a crater after a single break operation.

Sample	$S_q/\mu m$	$S_{\nu}/\mu m$	$S_p/\mu m$	$S_z/\mu m$	S_{sk}
Ag/Ni 90/10	1.12 ± 0.12	12.21 ± 4.51	10.64 ± 2.31	22.85 ± 6.78	0.27 ± 0.27
Ag/SnO ₂ 92/8	0.68 ± 0.08	8.11 ± 1.38	9.75 ± 2.39	17.86 ± 3.00	$\boldsymbol{1.27 \pm 1.04}$
Ag/SnO ₂ 90/10	0.65 ± 0.08	$\textbf{5.44} \pm \textbf{0.62}$	7.36 ± 1.28	12.80 ± 1.80	$\boldsymbol{0.72 \pm 0.44}$
Ag/SnO ₂ 88/12	$\boldsymbol{0.62 \pm 0.04}$	6.25 ± 1.31	7.73 ± 1.89	13.97 ± 3.05	$\textbf{0.66} \pm \textbf{0.46}$
Ag rod	$\boldsymbol{0.99 \pm 0.04}$	6.56 ± 0.26	7.31 ± 1.70	13.87 ± 1.55	0.13 ± 0.03
Ag 0 %	0.96 ± 0.07	$\textbf{7.99} \pm \textbf{1.43}$	6.26 ± 0.15	$\textbf{14.24} \pm \textbf{1.44}$	-0.10 ± 0.26
Ag 1 %	$\boldsymbol{0.98 \pm 0.09}$	$\boldsymbol{8.59 \pm 0.37}$	8.52 ± 0.35	17.11 ± 0.61	0.62 ± 0.12
Ag 2 %	0.99 ± 0.09	$\textbf{8.14} \pm \textbf{0.91}$	9.50 ± 0.43	17.64 ± 0.51	1.21 ± 0.34
Ag 3 %	1.32 ± 0.29	9.17 ± 1.10	11.95 ± 3.76	21.12 ± 4.58	$\textbf{0.64} \pm \textbf{0.57}$
Cu rod	0.65 ± 0.05	6.56 ± 1.13	5.96 ± 1.25	12.51 ± 1.91	0.39 ± 0.09
Cu 0 %	0.75 ± 0.03	8.76 ± 1.84	5.29 ± 0.33	14.05 ± 1.91	$\boldsymbol{0.08 \pm 0.20}$
Cu 1 %	1.05 ± 0.04	8.39 ± 1.01	8.83 ± 0.99	17.22 ± 0.85	$\boldsymbol{0.73 \pm 0.20}$
Cu 2 %	$\boldsymbol{0.97 \pm 0.06}$	7.96 ± 0.53	8.39 ± 0.94	16.35 ± 1.46	$\textbf{0.35} \pm \textbf{0.44}$
Cu 3 %	$\boldsymbol{1.27 \pm 0.02}$	$\boldsymbol{9.27 \pm 0.98}$	10.77 ± 1.31	20.05 ± 1.72	$\textbf{0.59} \pm \textbf{0.35}$

Relays, contactors, and other switching components are subjected to numerous make and break operations. As a result, the contacting surfaces are constantly being modified due to the topographic changes generated by the electrical arc. Therefore, the morphology of the resulting crater after a break operation is of particular interest. Understanding the topographic changes produced by the electrical arc enables the prediction of the contact physics for the subsequent make operations. Accordingly, the Abbott-Firestone curves and the corresponding parameters were determined to gather information on the peak and valley distribution, further complementing the topographic parameters shown in Table 3 [56-58]. The curves and parameters were determined for at least three arc erosion craters per sample type. The Abbott-Firestone curves for an arc erosion crater are shown in Supplementary Figure 1, with the corresponding parameters presented in Table 4. This figure and table present the results from a single crater per sample type, corresponding to the craters micrographed (shown in Fig. 1 and Supplementary Figure 5). These craters are representative of all the arc erosion craters, with variations that do not exceed 20 % (except for 3 wt% samples). Moreover, topographic information of the samples' surface after arc erosion is further presented in Supplementary Figure 2, Supplementary Figure 3, and Supplementary Figure 4. These figures depict a three-dimensional view of the crater's morphology of all samples and counter electrodes, as well as the height distribution of each sample's crater.

As the Abbott-Firestone parameters in Table 4 show, the core roughness depth – i.e., load bearing volume, R_k – of the MMC tends to be higher than that of the reference materials. As previously observed, the 3 wt% samples perform significantly differently compared to the MMC with lower CNT contents. As Table 4 shows, the core roughness depth of Ag 3 % and Cu 3 % are over 200 % greater than their unreinforced counterparts, indicating a much rougher load bearing area. This may be beneficial for electrical conductivity during subsequent make operations, as the increased number of asperities (as also observed in Table 2 and Table 3) promotes plastic deformation, thereby enlarging the contact area and reducing constriction resistance [59].

The copper rod sample, for example, exhibits the lowest core roughness depth among the evaluated craters, indicating a smooth core surface after arcing. Observing the reduced peak height (R_{pk}) and reduced valley depth (R_{vk}) for the crater and recalling the roughness parameters from Table 3, it is clear that the energy input did not produce significant topographic changes in this reference material. This sample also presents the lowest higher material ratio (M_{r1}) and lower material ratio (M_{r2}) . These parameters represent the amount of material above (asperities) and below (valleys) the core material [57,60,61]. After the arc erosion test, the copper rod sample exhibits only 15.1 % of material above the load bearing volume, the lowest amount among all the samples herein analyzed. The M_{r2} , on the other hand, is similar to that of the other samples. Contrarily, the silver rod sample exhibits an R_k , $R_{\nu k}$, $R_{\nu k}$, M_{r1} , and M_{r2} that is greater than the unreinforced silver and MMC containing up to 2 wt%. This indicates that the addition of the reinforcement phase in silver MMC favors a smoother transition from peak heights to core material and from core to valley depths.

These exemplary Abbott-Firestone parameters validate the displaced volumes and roughness parameters presented in Table 2 and Table 3. The resulting surfaces after a single break operation of the proposed MMC are similar to that of the reference silver-based materials. Therefore, the incorporation of CNT into the silver and copper matrices – up to 2 wt% in concentration – does not significantly change the resulting surface in comparison to the reference materials. Therefore, the load-bearing capacity of the proposed electrodes should perform similarly to the reference materials in subsequent make and break operations.

SEM micrographs and the corresponding EDS mappings of the craters after a break operation were acquired. An SEM micrograph and EDS map of an arc erosion crater for the reference samples, Ag rod, Ag 0 %, Ag 3 %, Cu rod, Cu 0 %, and Cu 3 % are shown in Fig. 1. The SEM micrograph and EDS map of the remaining samples are shown in

Supplementary Figure 5. Furthermore, Supplementary Figure 6, Supplementary Figure 7, and Supplementary Figure 8 show SEM micrographs highlighting features of the re-solidified material, as well as a carbon-gold EDS map overlay of the entire crater. This EDS overlay provides further information on the transfer of the gold trace material from the cathode towards the anode. It is important to note that EDS was not used for quantitative analysis of gold content transferred towards the anode, but rather to identify regions affected by material transfer.

The shape, size, amount of material transfer, and morphology of the re-solidified metal on the reference materials (Fig. 1a, b, c, and d) are similar. In general, the craters have a noncircular shape, suggesting arc motion. All reference samples show a considerable amount of material transferred from the counter electrode towards the sample electrodes, as indicated by the large surfaces where gold signal was detected in the EDS maps. Particularly in the Ag/SnO₂ samples, lower tin oxide content presented larger areas with deposited gold. Interestingly, the gold signals are not centered within the crater but rather surrounding the severely eroded regions. Based on the SEM micrographs and EDS maps, it can be hypothesized that the areas with stronger gold signals are the regions where the arc was ignited. As the arc ignites, the temperature quickly rises, leading to the melting of the metals. In the silver-based samples, silver melts before the hard gold coated counter electrode, whereas in the copper-based samples the gold counter electrode melts before the matrix. Therefore, it can be hypothesized that after the ignition of the arc, gold is no longer deposited, and the samples are eroded by ion and electron bombardment. This would explain why the gold signals in the EDS mappings are found primarily surrounding the crater rather than within the crater. This hypothesis can, in part, be validated by observing the protruding gold signals (relative to the center of the craters) highlighted by the black arrows in the Ag/Ni 90/10 and Ag/SnO2 92/8 samples (Fig. 1a and b). In these samples, high-speed camera footage and the I-V and power curves prove the presence of unstable arcing [28]. Consequently, multiple small electrical arcs ignited on the surface, thereby producing multiple protrusions rather than one. Nevertheless, these hypotheses cannot be fully validated by the EDS maps alone, requiring further investigation into the mechanisms behind gold's transfer.

As is the case with the silver-based reference materials, the silver rod sample and the unreinforced sintered silver sample (Ag 0 %) show considerable gold transfer (Fig. 1e and f). The transferred material is primarily located on one side of the crater, with minimal gold intensity scattered within the crater. The reinforced sample (Fig. 1g), on the other hand, presents a more uniform gold deposition within the crater. Since the Ag 0 % and Ag 3 % sample present similar hardness values, it can be assumed that both have similar contact areas once the normal load was established. Therefore, the more uniform transfer of material may be caused by the ignition of a wider arc in the initial instances of the break operation. It is reasonable to assume that a wider arc ignites in the reinforced sample due to the elasticity of the reinforcement phase, which remains in electrical contact with the counter electrode as the rivet recedes and the CNT restitute to their original position. Another possible explanation is the confinement of the arc, reducing the chances of it igniting in one spot and moving throughout the sample (and thus eliminating the protruding gold signal). Moreover, the EDS map in Fig. 1g-ii showcases the presence of large CNT clusters throughout the crater, whereas the surrounding regions present significantly smaller CNT agglomeration. As the electrode's material melts during arcing, the CNT on the surface of the electrode re-agglomerate and tend to move towards the surface of the electrode on account of the density difference between the molten metal and the reinforcement phase (10.49 and 1.92 g/cm³ for silver and pristine multiwalled CNT, respectively [1, 62]), analogous to flocculation in colloids.

The high mobility of the arc is easily verified by observing the arc erosion crater of the copper rod sample (Fig. 1h) – and further supported by the high-speed video footage from [28]. On this sample, the arc was ignited on the bottom right of the micrograph, where high intensities of

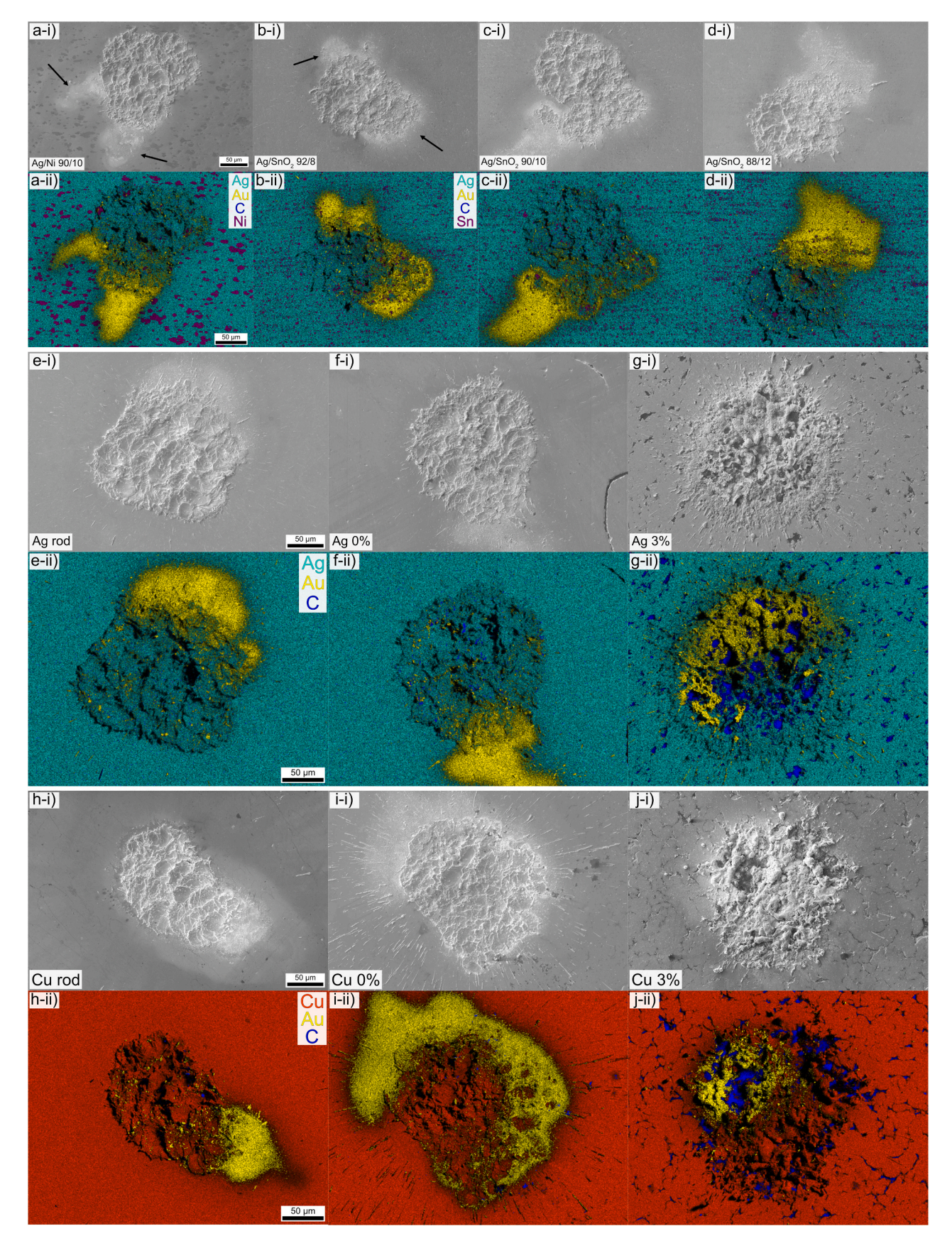


Fig. 1. i) SEM micrograph and ii) EDS map of a) Ag/Ni 90/10, b) Ag/SnO₂ 92/8, c) Ag/SnO₂ 90/10, d) Ag/SnO₂ 88/12, e) Ag rod, f) Ag 0 %, g) Ag 3 %, h) Cu rod, i) Cu 0 %, and j) Cu 3 %. The black arrows highlight gold protruding from the center of the crater, indicating potential multiple arc ignition sites. Black regions within the crater in the EDS maps are areas where no signal was detected due to shadowing effects as a result of the crater's topography.

gold were detected. As the inter-electrode gap grew, the arc moved upwards towards the left of the micrograph. Furthermore, the varying size of the crater indicates that as the arc moved it also widened. The unreinforced sintered copper sample (Fig. 1i) experienced more material transfer compared to the copper rod sample. Considerable amounts of gold were detected surrounding the arc erosion crater. However, the size and shape of the crater suggests that the arc did not move as much as in the Cu rod sample, possibly due to the lower hardness of the sintered sample. The crater of the Cu 3 % sample (Fig. 1j) presents the lowest gold intensities among the copper samples. As was observed in the Ag 3 % sample, larger CNT clusters are observed within the crater. However, in this case the degree to which CNT re-agglomerate is not as significant since the reinforcement phase distribution prior to arc is more heterogeneous [28,30]. Moreover, the SEM micrographs of both reinforced samples (Fig. 1g and j) illustrate the increased topographic features generated due to arcing - as previously described in Table 2, Table 3, and Table 4.

A FIB cross section was conducted on the arc erosion crater of a silver and a copper MMC to observe the buckling of the surface beneath the resolidified and re-deposited material following the break operation. In addition, the cross sections facilitate a depth-resolved visualization of the state of the reinforcement phase beneath the crater. The micrographs corresponding to the cross sections conducted on the Ag 2 % and Cu 2 % samples are shown in Fig. 2. As illustrated in the micrograph and inset (Fig. 2a), the silver MMC sample exhibit minimal buckling beneath the arc erosion crater. A slight depression in the surface's datum line was discerned in the vicinity of the crater's center, yet the surrounding regions of the cross section exhibited no indications of alterations - as previously described by the S_{sk} parameters (Table 3). Upon examination of the magnified micrograph of the Ag 2 % sample (Fig. 2b), it can be observed through the presence of CNT on the crater surface - highlighted by the violet arrows – that the reinforcement phase endured the electrical arc. It can thus be inferred that subsequent make and break operations will yield comparable electrical performance and arc

behavior as in the first break operation given the presence of CNT on the contacting site [28]. Unaffected clusters of CNT are observed beneath the crater, as indicated by the orange arrows in Fig. 2b. In comparison to the CNT situated on the surface, the clusters beneath the crater exhibit a higher contrast with the matrix, whereas the superficial CNT are a light shade of gray. The alteration in contrast may suggest a degree of amorphization resulting from the electrical arc, which reduces the conductivity of the CNT, thereby changing the contrast in the SEM micrograph. Furthermore, the deposition of small-scale metallic droplets originating from the formation of metallic vapor upon the explosion of the molten bridges could also favor a lighter shade of gray for the CNT situated on the surface of the crater. The cross section not only exhibits small-scale droplets, but also demonstrates that larger metallic droplets were deposited on the reinforcement phase, as indicated by the dashed green circles and shown in Supplementary Figure 9a. These droplets are pervasively found re-deposited throughout the surface of the crater, coating the re-solidified metal and the CNT on the surface – as indicated by the red arrows in Supplementary Figure 9a. Moreover, the yellow arrows in Fig. 2b highlight the presence of pores within the silver MMC. Nonetheless, these pores are not devoid of material. The perimeter of the highlighted voids have adhered CNT. Specifically, the void on the right has a CNT extending radially from one end of the void to another. The FIB cross sections shown in Fig. 2 also reveal that the re-agglomeration of the reinforcement phase previously observed in the SEM micrographs and EDS maps (Fig. 1) is not as significant as initially believed. This is evidenced by the similarity in agglomerate sizes on the surface (or directly below it) compared to those considerably below the surface. Moreover, Fig. 2b shows a certain degree of CNT that surfaced due to different density values between the reinforcement phase and the molten matrix. Nevertheless, the surfaced CNT film is thin, with thicknesses that do not exceed 1 μm (in regions that are not associated to an underlying CNT cluster).

Contrarily to what was observed in the silver MMC, the copper MMC (Fig. 2c) does not present significant amounts of CNT on the surface of

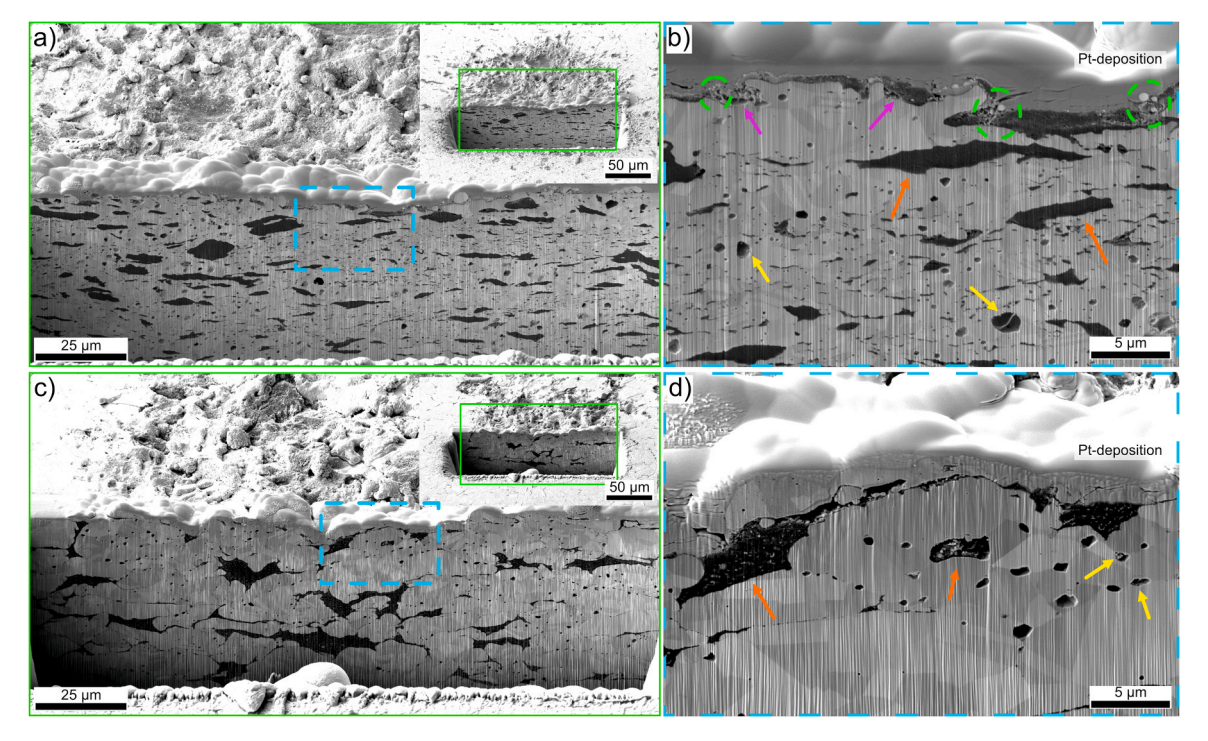


Fig. 2. a) FIB cross section and b) magnified micrograph of the cross section near the surface of the Ag 2 % sample. c) FIB cross section and d) magnified micrograph of the cross section near the surface of the Cu 2 % sample. The green squares show the region of interest in the cross section, whereas the cyan dashed squares highlight a magnified region near the surface beneath the crater. The violet arrows indicate carbon content on the surface of the crater that may have been affected by the arc, the orange arrows show unaffected CNT beneath the crater, and the yellow arrows point out voids within the MMC. The green dashed circles highlight metallic vapor re-deposition on the reinforcement phase.

the crater. The silver MMC exhibits a thin, yet pervasive layer of CNT uniformly distributed across its surface, creating an even and consistent coverage. In contrast, the copper MMC demonstrates minimal presence of CNT, with the nanotubes appearing in clustered formations due to their agglomeration. Nevertheless, the CNT clusters observed are not related to re-agglomeration during arcing, but rather are clusters formed during MMC manufacturing. The stark difference in distribution highlights the superior dispersal of CNT on the silver matrix compared to the copper [28]. The tendency of CNT to agglomerate, in addition to the lower chemical compatibility between copper and carbon, has led to uneven and sparse coverage, with regions devoid of CNT and regions with CNT large clusters. The cross section of the copper MMC also demonstrates the increased buckling present in this metallic matrix. The depression of the surface below the datum is higher than in silver, showing a particularly higher depression at the center of the crater. Nonetheless, the region with the highest depression coincides with a CNT cluster which could further promote buckling of the surface although there is a thin layer of copper between the surface of the crater and the CNT cluster. Recalling the average S_{sk} values for copper samples (Table 3), these samples presented the most symmetrical crater topographies. Furthermore, the average displaced volumes (Table 2) also indicate marginal buckling of the copper craters. A possible explanation for the depression in the FIB cross section may be that material transfer – i.e., re-deposition of metallic vapor - is more significant in the topographic maxima on the copper electrode. Thereby producing high peaks and low valleys. However, this is likely not the case, since the S_{ν} , S_{D} , and S_z parameters are within the same range as in the silver MMC (Table 3). Since FIB is a highly localized technique, the more significant depression

at the center of this crater may not be fully representative of all copper-based samples. It is reasonable to assume that the buckling in the cross section is due to the aforementioned CNT cluster close to the surface of the crater.

The magnified micrograph of the Cu 2 % sample's cross section (Fig. 2d) highlights the presence of voids, voids encompassing CNT (yellow arrows), and the presence of large CNT bundles beneath the arc erosion crater (orange arrows). The magnified micrographs in Fig. 2d and Supplementary Figure 9b highlight the absence of condensation droplets at the interface originating from the metallic vapor after the explosion of the molten bridge. Nonetheless, as the red arrows in Supplementary Figure 9b demonstrate, the surface of the crater shows an undulating surface, likely caused by re-deposition. However, droplets were not discernible on the cross section, as was the case with the silver sample. Moreover, the violet arrows in Supplementary Figure 9b highlight the presence of CNT within open porosities on the crater's surface.

Moreover, FIB cross sections of the arc erosion craters for the sintered reference samples (i.e., Ag 0 % and Cu 0 %), as well as the 1 wt% and 3 wt% silver and copper MMC are shown in Supplementary Figure 10. These cross sections show similar performance as those shown in Fig. 2. That is, the re-deposition of metallic droplets on the silver samples and the pervasive coverage of a thin CNT film in the Ag 3 % sample. As with the Ag 2 % sample, the thin CNT film also shows a lighter contrast compared to those beneath the affected zone, indicating a certain degree of amorphization. This is also the case in the copper MMC, however, to a lower extent.

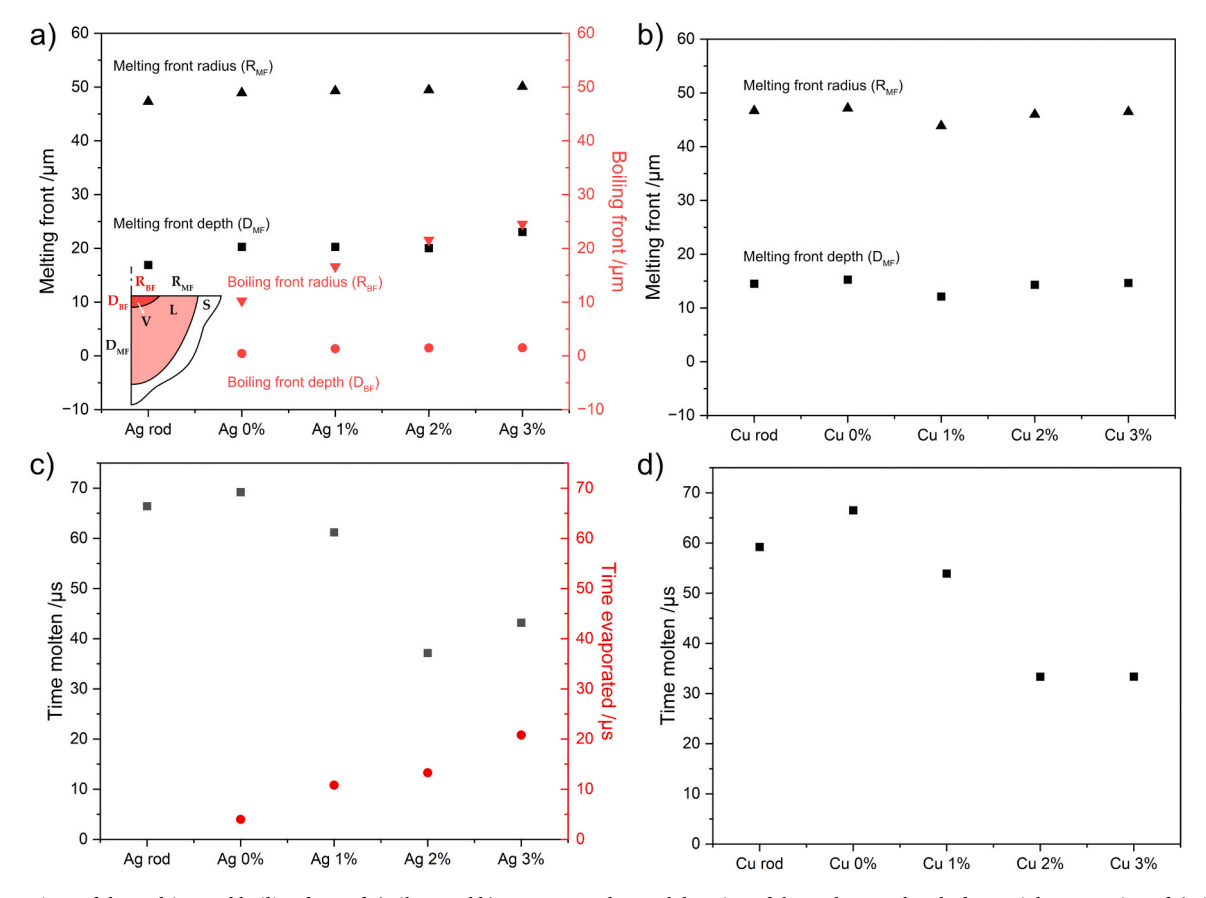


Fig. 3. Dimensions of the melting and boiling from of a) silver and b) copper samples; and duration of the molten pool and of material evaporation of c) silver and d) copper samples. The inset in a) schematically represents the dimensions of both fronts. Each front can be portrayed as a quarter ellipsis, forming the volume as a solid of revolution along the y-axis. In this inset, the letters V, L, and S indicate the metal's phase – i.e., vapor, liquid, and solid, respectively. Note: in a) and c), the Ag rod sample did not undergo material evaporation.

3.2. Thermal simulations

The results thus far emphasize the exceptional performance of the proposed MMC (up to CNT concentrations of 2 wt%). However, to further delve into the influence of the reinforcement phase on the arc erosion performance, thermal simulations were carried out. The simulations provide information on the dimensions of the affected volume, maximum temperature reached by the electrodes, and duration of the molten pools and material evaporation. The radius of the melting front (shown in Fig. 3a and b) highlights the fact that the addition of the reinforcement phase, as well as the increment in its concentration, does not imply a wider melting front. Irrespective of CNT content, the melting front has a radius of approximately 49 μm and 46 μm for silver and copper matrices, respectively. Likewise, the depth of the melting front does not appear to be significantly affected, with silver and copper matrices showing average melting front depths of approximately 20 µm and 14 µm, respectively. As was presented in Table 1 and shown in Fig. 1 and Supplementary Figure 5, the thermal simulations confirm that the area affected by the arc is smaller in copper matrices than in silver matrices. Similarly, the volume displaced below the datum line in Table 2 can be explained by the smaller melting front depth simulated for the copper matrices compared to silver matrices. It should be noted, however, that any discrepancies between the thermal simulations and the results from the CLSM and SEM analysis are due to the aforementioned simplifications in the simulations. Nonetheless, the heat affected zone obtained in the thermal simulations is in agreement with those observed in the FIB cross sections (presented in Fig. 2). Furthermore, the results from the thermal simulations validate the hypothesis that the higher degree of buckling observed in the cross section of the copper MMC is due to the presence of the CNT cluster, as opposed to increased re-deposition and/or material transfer at the topographic maxima.

The thermal simulations prove that the copper-based materials did not exceed 2600 K. Therefore, since the boiling temperature of copper was not exceeded, these electrodes did not experience material evaporation. This result from the simulation justifies why the copper samples exhibit the most symmetrical topographic features, presenting S_{sk} values that approach zero (Table 3). Furthermore, the lack of small-scale metallic droplets observed in the FIB cross section (Fig. 2c and d) is validated by the thermal simulations. Since the copper electrodes did not reach a temperature that exceeded its boiling point, it is not possible for metallic vapor to be re-deposited on the electrode's surface. The silver electrodes, on the other hand, reached maximum temperatures of 2550 K, exceeding the boiling temperature of silver by over 100 K. A notable outlier is the high-purity silver sample (i.e., Ag rod), which did not reach the boiling temperature and therefore did not exhibit a melting front. The lower temperature of the Ag rod electrode is expected to be due to the instability of the electrical arc (refer to the power curves in [28]). Since in this sample the electrical arc ignites and extinguishes multiple times during the break operation, the there is enough time for the electrode to slightly cool down between unstable arcing. Furthermore, the maximum temperatures reached during arcing are insufficient to sublimate the reinforcement phase, falling well below the boiling temperature of carbon.

The boiling front depth exhibits an average value of 1 μ m for all sintered silver samples. As is the case with the melting front dimensions, the concentration of the reinforcement phase does not influence the boiling front's depth. The width of the boiling front, on the other hand, does change. As the CNT content increases, so does the radius of the boiling front. The sintered unreinforced silver sample (i.e., Ag 0 %) exhibits an approximate boiling front radius of 10 μ m, whereas the Ag 3 % samples 24 μ m. The higher amounts of material evaporation justify the higher volumes below the datum line of the craters shown in Table 2, as well as the higher S_{ν} , S_{p} , and S_{z} shown in Table 3 and R_{k} in Table 4.

The duration of the molten pools and material evaporation are shown in Fig. 3c and d. Both metallic matrices show the same trend, a slight increase in molten pool duration between the rod references and

the sintered references. As the concentration of the reinforcement phase increases, a noticeable reduction in molten pool duration is observed. Incorporating 1 wt% of CNT does not produce significant reductions. However, 2 wt% and 3 wt% CNT content incurs faster re-solidification of the molten pool due to the increased thermal diffusivity of the electrode. The faster re-solidification process observed in the thermal simulations can be verified with the CLSM measurements (Table 2 and Table 3). The samples that re-solidify faster are the samples that present the highest S_p , S_z , and volume displaced above the datum line. In the sintered silver samples, there is a clear correlation between CNT content, width of the boiling front, and duration of evaporation. These samples show that, as the concentration of CNT increases, so does the width of the boiling front, which consequently leads to a longer duration of material evaporation. This is likely due to the fact that the electrical arcs generated are more stable and less mobile. Consequently, the constant and more concentrated arc does not allow the temperature of the electrode to reduce below its boiling temperature - refer to I-V and power curves in [28].

3.3. CNT structural characterization

Raman spectroscopy was carried out after arc erosion tests on the CNT within the crater to evaluate the structural damage that the reinforcement phase might have sustained due to arcing. The Raman spectrum of CNT in unaffected areas were also obtained, as well as the spectrum of pristine CNT as reference. The Raman spectra within and outside of each crater for each sample type are shown in Supplementary Figure 11 and Supplementary Figure 12.

The Raman spectrum of pristine CNT features their characteristic D-, G-, D', and G'-bands. The D-band, usually observed at a Raman shift of 1350 cm⁻¹, corresponds to the A_{1g} symmetry breathing mode [53,63]. This mode is only activated in the presence of defects in the carbon structure. The (G+D')-band is the result of the convolution of the G- and D'-bands [53]. This convoluted peak is a prominent feature in the Raman spectrum of CNT [64]. The G-band, observed at a Raman shift of 1581 cm $^{-1}$, is associated with the $E_{2\,g}$ phonon mode [53]. In pristine CNT, the (G+D')-band shows a distinct shoulder at higher wavenumbers due to the defect-induced double resonance, leading to the D'-band appearing between 1617 cm⁻¹ and 1625 cm⁻¹ [53]. Like the D-band, the D'-band is activated by crystalline defects. Increments in the D'-band represents the transition from a monocrystalline to a polycrystalline state [53]. The dispersive G'-band appears approximately 2700 cm⁻¹ and arises from a second order scattering process. As an overtone of the D-band, the G'-band indicates long-range order and fades with increasing degradation or amorphization [65].

The G-band is a non-dispersive peak [53]; consequently, its position does not depend on the excitation energy of the laser used for Raman spectroscopy. Accordingly, Ferrari and Robertson proposed a way of identifying the level of degradation in carbon by tracing the defect ratio (I_D/I_G) and the position of the G-band [53]. A three-stage phenomenological model for the amorphization of graphitic carbon was developed, where the first stage comprises the transition from graphite to nanocrystalline graphite. Within this stage, the G-band's position moves between 1581 cm⁻¹ to 1600 cm⁻¹. The G-band position of the pristine CNT and of CNT clusters outside and inside the arc erosion craters are shown in Fig. 4a. As the plots present, there is a slight upshift in wavenumber comparing the state of the CNT clusters outside and inside the craters. The upshift is related to the appearance and development of the D'-band at approximately 1620 cm⁻¹. Nonetheless, the upshift is marginal, with the Raman shift values remaining within the theoretical range, highlighted by the shaded area. Therefore, the position of the G-band indicates that the sp^2 graphitic carbon structure remains without reaching the amorphization state (stage 3 as proposed by Ferrari and Robertson [53]). However, the upshift suggests a slight tendency towards a nanocrystalline graphitic carbon structure - which corresponds to stage 2 in the amorphization trajectory. Moreover, comparing the

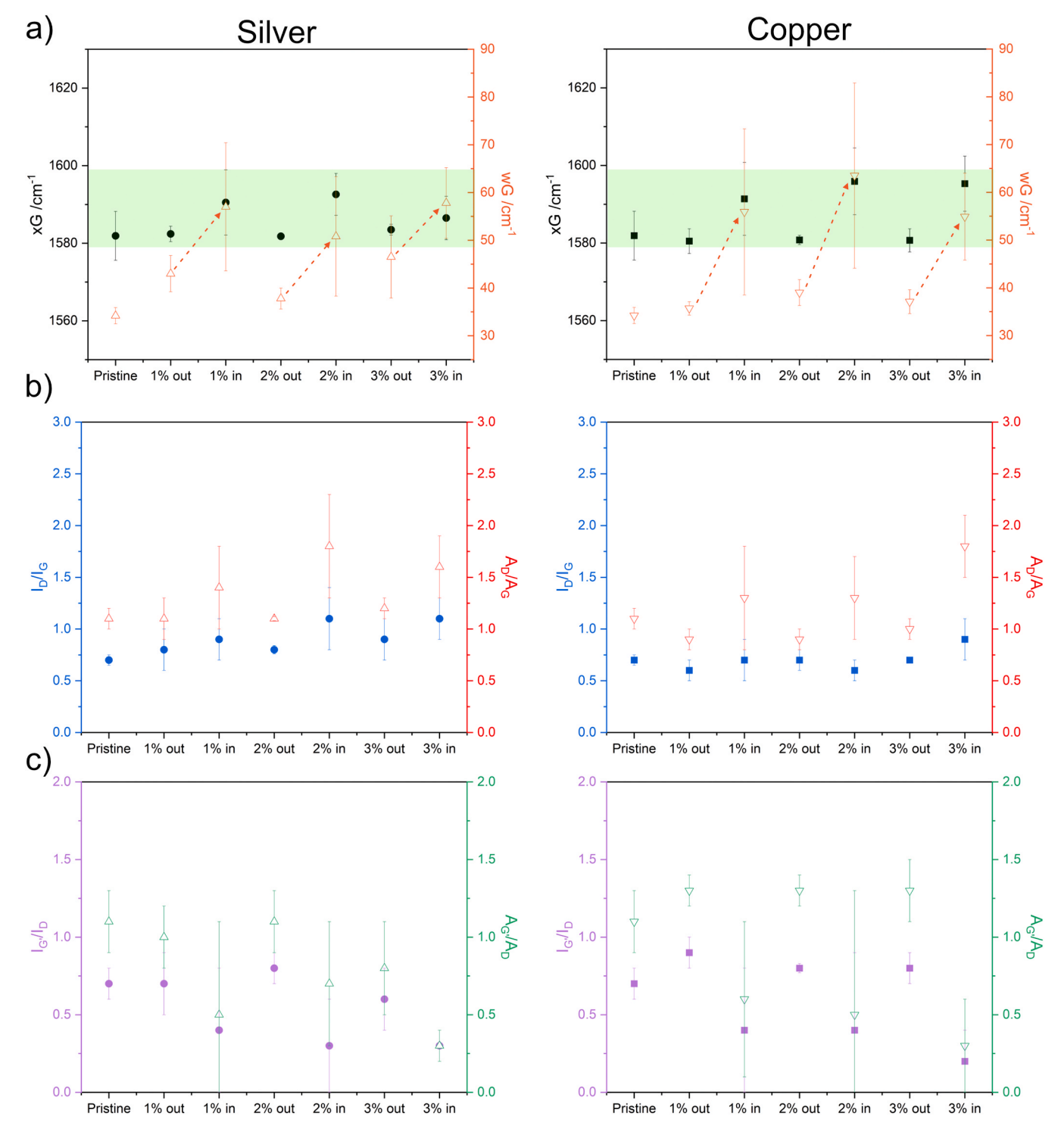


Fig. 4. a) Raman shift and FWHM of the G-band (xG and wG), b) defect and c) purity indeces of pristine CNT, CNT outside, and CNT inside the arc erosion crater of silver (left) and copper (right) MMC. The shaded region in a) highlights the theoretical position of the G-band of graphitic carbon, as reported by Ferrari and Robertson [53]. The dashed arrow emphasized the widening of the G-band (i.e., increased FWHM) after arc erosion tests, indicating the appearance of crystallographic defects in the structure of the CNT after arcing. Note: the intensity and integral intensity defect ratio inside the crater in Ag 3 % are identical (i.e., 0.3 ± 0.1).

Raman shift of the G-band (xG) measured outside of the arc erosion craters (unaffected region) with those of the pristine CNT demonstrates that the manufacturing process of the MMC does not affect the sp^2 graphitic structure of the CNT.

The full width at half maximum (FWHM) of the G-band (wG) is of interest since the width of this band provides insight into the structural integrity of the CNT. Raman spectroscopy is a harmonic oscillator system based on the inelastic scattering of photons. Thus, considering the

graphitic structure of the CNT as a harmonic resonator, structural defects (such as a missing carbon atom) will affect the oscillation half-time of the graphitic structure. Therefore, a narrower G-band (low energy and longer oscillation times according to the uncertainty principle) indicates higher crystallinity of the CNT [66]. Conversely, a wider G-band (higher energy and shorter oscillation times) suggests that increased crystallographic defects are present in the CNT's structure. The FWHM of the G-band (shown in Fig. 4a) suggests increased defects in the CNT after arc

erosion tests. This is evidenced by the broadening of the peak (highlighted by the dashed arrow), which could be caused by the adsorption of oxygen atoms during arc erosion tests.

Both defect ratios (i.e., intensity and integral intensity) for the pristine CNT and all MMC are shown in Fig. 4b. As previously suggested by the position of the G-band, the defect ratios confirm that the sintering process did not significantly affect the structural integrity of the CNT, since all values are very close to that of the pristine state. Interestingly, the CNT that were exposed to the electrical spark (inside the crater) show marginal increase in their I_D/I_G indices, being the highest value observed for the silver-based MMC. The most likely degradation processes undergone by the CNT are amorphization and oxidation, due to the meaningful energy input [67]. Since the experiments were carried out in an uncontrolled environment (i.e., atmospheric conditions), oxygen is readily available in the vicinity of the molten pool. This adsorption of oxygen by the CNT in the silver-based MMC is likely the cause of the lighter contrast of superficial CNT in the SEM micrographs from Fig. 2a and b, Supplementary Figure 9, and Supplementary Figure 10. In both areas (within and outside of the arc erosion crater), the CNT in silver matrices exhibit higher I_D/I_G ratio than the pristine CNT. The CNT in the copper matrices, on the other hand, exhibit similar or even lower I_D/I_G ratio than the as-received CNT. This can be explained by the fact that copper is able to intake the available oxygen. Therefore, the CNT in the copper matrices do not undergo oxidation, with the matrix itself being selectively oxidated. This is not only verified by the I_D/I_G ratio, but also due to the lack of contrast change in the SEM micrographs (Fig. 2, Supplementary Figure 9, and Supplementary Figure 10). This hypothesis is further verified by the appearance of a peak in the Raman spectra acquired inside the crater for the copper MMC (highlighted by the orange arrow in Supplementary Figure 12). Based on the Raman shift of this peak (approximately 620–630 cm⁻¹), it is likely that CuO and/or Cu₂O are formed inside the crater [68,69]. EDS maps focusing on large CNT clusters both inside and outside of the crater were acquired for both metallic matrices. However, no discernible differences were observed in the oxidative state of the CNT or surrounding matrix. SEM micrograph and EDS map of CNT clusters inside and outside of the arc erosion crater in the Ag 3 % and Cu 3 % samples are shown in Supplementary Figure 13 and Supplementary Figure 14, respectively.

The integral intensity defect ratio encompasses all types of defects, whereas the intensity defect ratio does not. Consequently, the A_D/A_G ratio in each measurement spot is higher than the I_D/I_G ratio. Comparing the integral intensity defect ratio of the pristine CNT with those of the CNT clusters outside of the arc erosion crater shows that the sintering process does not cause any previously unaccounted type of damage onto the structure of the CNT, since the same trend as with the intensity defect ratio is observed. Focusing on the defect state of the CNT outside and inside the craters, the A_D/A_G ratio shows similar damage after arcing irrespective of the metallic matrix. However, this is not the case for the I_D/I_G ratio. The I_D/I_G ratio increases in silver matrices and remains constant in copper matrices. As previously discussed, the constant intensity defect ratio observed for copper matrices is due to the oxidation of the matrix rather than the reinforcement phase. Therefore, I_D/I_G is more sensitive to oxidation than A_D/A_G .

The purity of the multi-walled CNT can be assessed by determining the intensity and integral intensity of the G'- and D-bands ($I_G \cdot / I_D$ and $A_G \cdot / A_D$), as proposed by DiLeo et al. [65,70,71]. The purity indices for pristine CNT and CNT clusters outside and inside the arc erosion crater are shown in Fig. 4c. The purity indices in the silver-based MMC do not show any noteworthy difference between the pristine state and the state outside the crater. In the copper-based MMC, on the other hand, a marginal improvement in the purity indices is observed. Therefore, the purity indices demonstrate that the manufacturing process does not affect the purity of the reinforcement phase. On the other hand, the purity drops markedly within the craters for all the studied composites due to the arc's energy input.

4. Conclusions

Arc erosion tests operating at 200 W ohmic load were carried out on standard switching materials, pure silver and copper, and CNT-reinforced silver and copper MMC manufactured via powder metallurgy. Morphological, topographic, and chemical characterization of the crater resulting from a single break operation was carried out. In addition, the structural integrity of the reinforcement phase after arc erosion tests was conducted. Moreover, thermal simulations were performed to determine the affected volume, maximum temperature reached by the electrode, and molten pool and material evaporation duration.

Morphological characterization revealed that silver and copper MMC with up to 2 wt% CNT exhibit craters with similar dimensions and displaced material volumes, whereas higher CNT concentrations (i.e., 3 wt%) resulted in larger craters with higher amounts of displaced material volumes. This, in turn, affected the roughness and load-bearing capacity of these MMC. CNT concentrations below 3 wt% resulted in roughness values similar to that of the reference materials, whereas samples with CNT concentrations of 3 wt% exhibited higher roughness and a higher proportion of material above the core load-bearing volume – particularly the silver sample. Moreover, the dimensionality of the crater in the reinforced samples tends to be more circular, highlighting the lower mobility of the arc due to the confining effect of the reinforcement phase.

Finite element thermal simulations proved that the temperatures reached for the copper electrode were not sufficient to evaporate the metallic matrix, as well as being far below the sublimation temperature of CNT. The sintered silver samples, on the other hand, did surpass the boiling temperature of the matrix, thus leading to material evaporation. Irrespective of CNT content, the dimensions of the melting front remained relatively constant throughout all samples. Moreover, CNT contents above 1 wt% significantly reduced the duration of the molten pool to approximately 50 % the duration of the unreinforced samples. Nevertheless, increasing the concentration of the reinforcement phase in silver matrices led to larger boiling fronts and longer duration of material evaporation.

Raman spectroscopy revealed that the MMC manufacturing process did not affect the structural integrity nor the purity of the reinforcement phase. Although the arc's energy input did affect crystallinity and purity of the CNT, the damage sustained by the CNT was not enough to degrade the CNT into amorphous carbon. In the silver MMC, the CNT exhibit slight oxidation due to the matrix's limited oxygen intake, in contrast to the copper matrices, where higher I_D/I_G ratios indicate more pronounced CNT degradation. This confirms the reduced conductivity of the surface-exposed CNT in the silver MMC, as observed in the FIB cross sections.

Based on the findings herein reported, CNT concentrations of up to 2 wt% result in optimal switching performance in silver- and copperbased MMC. Increasing the concentration of the reinforcement phase affects both crater roughness and volume of displaced material after switching. This may accelerate electrode erosion, as previously reported for graphite-containing electrodes. Thermal simulations further confirmed this behavior, showing that the silver-based MMC exhibited a larger boiling front, despite having a consistent melting front and a shorter molten pool duration. Nevertheless, the addition of the reinforcement phase (up to 2 wt%) into silver and copper matrices results in composite materials that perform similarly to reference and standard switching materials. Simultaneously, they incorporate the benefits of carbon nanostructures, including low and stable contact resistance in the closed state and stable arcing behavior during breaking. These materials also help confine the electrical arc and reduce the need for metallic powders, thereby lowering weight and costs. Moreover, the proposed MMC can be manufactured in a straightforward, easily scalable, cost-effective, and standard method, with the capability of producing near-net-shape electrodes. The results presented in this work, along with the previously discussed benefits of the reinforcement phase,

underscore the potential of CNT-reinforced silver and copper metal matrix composites. In particular, the exceptional performance of the copper-based MMC demonstrates the effectiveness of CNT in enhancing the switching performance of this low-cost, highly conductive metal – enabling it to perform comparably to silver-based alloys and composites.

CRediT authorship contribution statement

Sebastian Suarez: Writing – review & editing, Supervision, Project administration, Methodology, Funding acquisition, Formal analysis, Conceptualization. **Frank Mücklich:** Resources, Project administration, Funding acquisition. **Francisco A. Delfin:** Writing – review & editing, Investigation. **Bruno Alderete:** Writing – original draft, Visualization, Validation, Methodology, Investigation, Formal analysis, Data curation, Conceptualization.

Declaration of Competing Interest

The authors declare that they have no known competing financial interests or personal relationships that could have appeared to influence the work reported in this paper.

Acknowledgements

B. A. wishes to acknowledge the support from the German Academic Exchange Service (DAAD) and the Roberto Rocca Education Program (RREP). F. A. D. acknowledges the financial support provided by the government of Upper Austria (Wi-2021–305611/21-Au / NaKuRe). The authors gratefully acknowledge funding in the Mat-Innovat ("Kreislauffähige Materialsysteme für in-novatives Hochleistungswerkstoffe") project, supported by the State of Saarland from the European Regional Development Fund (Europäischen Fonds für Regionale Entwicklung, EFRE). Funding for the PFIB/SEM instrument by German Research Foundation is greatly acknowledged (INST 256/510–1 FUGG).

Appendix A. Supporting information

Supplementary data associated with this article can be found in the online version at doi:10.1016/j.triboint.2025.110890.

Data availability

Data will be made available on request.

References

- Slade PG. Electrical Contacts. Second Ed. Boca Raton: CRC Press; 2014. https://doi. org/10.1201/b15640.
- [2] Jemaa NBen, Nedelec L, Benhenda S, Neveu J. Anodic and cathodic erosion of Ag, Ag alloys and Ag-MeO contact materials in energy range below 10 joules. In: Electrical Contacts - 1996. Proceedings of the Forty-Second IEEE Holm Conference on Electrical Contacts. Joint with the 18th International Conference on Electrical Contacts. IEEE: 1996. p. 70-4. https://doi.org/10.1109/HOLM.1996.557181.
- [3] Holm R. Electric Contacts. 4th Ed. Berlin, Heidelberg: Springer; 1967. https://doi. org/10.1007/978-3-662-06688-1 (Berlin Heidelberg).
- [4] Ben Jemaa N, Morin L, Benhenda S, Nedelec L. Anodic to cathodic arc transition according to break arc lengthening. IEEE Trans Compon Packag Manuf Technol Part A 2005;21:599–603. https://doi.org/10.1109/tcpma.1998.740053.
- [5] Swingler J, McBride JW. The net zero erosion phenomena on opening switching contacts with AC loading. In: Electrical Contacts - 1997 Proceedings of the Forty-Third IEEE Holm Conference on Electrical Contacts. IEEE; 1997. p. 238–45. https://doi.org/10.1109/HOLM.1997.638048.
- [6] Han J, Zhou Y, Li Z, Chen Y, Zhang Q. Effects of discharge current and discharge duration on the crater morphology in single-pulse arc machining of Ti6Al4V. Int J Adv Manuf Technol 2024;133:3367–81. https://doi.org/10.1007/s00170-024-13926-9.
- [7] Singh B, Saxena KK, Roy T. Opportunities and challenges in machining of aluminium metal matrix composites using electrical discharge machining. Proc Inst Mech Eng Part E J Process Mech Eng 2023. https://doi.org/10.1177/ 09544089231213861.
- [8] Braunovic M, Konchits VV, Myshkin NK. Electrical Contacts. 1st ed. Boca Raton, FL, USA: CRC Press; 2017. https://doi.org/10.1201/9780849391088.

- [9] Wang J, Duan C, Chen S, Hu H, Zhang Q, Chang Y, et al. Arc erosion behaviors and surface characteristics of SnO2 nanofiber/particle reinforced Ag-Based composite. J Mater Eng Perform 2024;33:4754–64. https://doi.org/10.1007/s11665-023-08300 x
- [10] Wang Y, Xu N, Wang L. Numerical simulation and analysis of contact erosion by high-current and low-voltage air arc considering the movement of arc. AIP Adv 2023;13. https://doi.org/10.1063/5.0144666.
- [11] Muitzel T, Niederreuther R. Advanced silver-tin oxide contact materials for relay application. In: 26th International Conference on Electrical Contacts (ICEC 2012). IET; 2012. p. 194–9. https://doi.org/10.1049/cp.2012.0647.
- [12] Behrens V, Honig Th, Kraus A, Mahle E, Michal R, Saeger KE. Test results of different silver/graphite contact materials in regard to applications in circuit breakers. In: Electrical Contacts - 1995. Proceedings of the Forty-First IEEE Holm Conference on Electrical Contacts. IEEE; 1995. p. 393–7. https://doi.org/10.1109/ HOLM 1995.482896
- [13] Michal R, Saegar KE. Metallurgical aspects of silver-based contact materials for air-break switching devices for power engineering. IEEE Trans Compon Hybrids Manuf Technol 1989;12:71–81. https://doi.org/10.1109/33.19015.
- [14] Wingert P, Bevington R, Horn G. The effect of graphite additions on the performance of silver-nickel contacts. In: Thirty-Sixth IEEE Conference on Electrical Contacts, and the Fifteenth International Conference on Electrical Contacts. IEEE; 1990. p. 524–9. https://doi.org/10.1109/HOLM.1990.113053
- [15] Shobert E. Carbon, graphite, and contacts. IEEE Trans Parts Hybrids Packag 1976; 12:62–74. https://doi.org/10.1109/TPHP.1976.1135101.
- [16] Jiang P, Li F, Wang Y. Effect of different types of carbon on microstructure and arcing behavior of Ag/C contact materials. IEEE Trans Compon Packag Technol 2006;29:420–3. https://doi.org/10.1109/TCAPT.2006.875873.
- [17] Wingert PC. The effects of interrupting elevated currents on the erosion and structure of silver-graphite. In: Electrical Contacts - 1996. Proceedings of the Forty-Second IEEE Holm Conference on Electrical Contacts. Joint with the 18th International Conference on Electrical Contacts. IEEE; 1996. p. 60–9. https://doi. org/10.1109/HOLM.1996.557180.
- [18] Xie W, Wu G, Yang Z, She P, Wang H, Zuo H, et al. Study on the erosion characteristics of copper-carbon electrode pairs by DC air arc. High Volt 2021;6: 674–83. https://doi.org/10.1049/hve2.12124.
- [19] Zhang L, Ye Q, Zeng X, Liu S, Chen H, Tao Y, et al. Preparation and properties of graphene reinforced copper electrical contact materials for high-voltage direct current electrical contacts. Electron 2023;13:53. https://doi.org/10.3390/ electronics13010053
- [20] Ding T, Chen GX, Li YM, Yang HJ, He QD. Arc erosive characteristics of a carbon strip sliding against a copper contact wire in a high-speed electrified railway. Tribol Int 2014;79:8–15. https://doi.org/10.1016/j.triboint.2014.05.003.
- [21] Song Y, Yang Z, Jiao J, Li W, Zhao M, Shangguan B, et al. Research on damage optimization of copper-carbon gradient composite materials for current-carrying friction. Tribol Int 2024;195:109635. https://doi.org/10.1016/j.triboint.2024.109635.
- [22] Wang P, Xie F, Wexler D, Yin J, Zhang H, Zhu H. Tribological behaviors of copper modified carbon/carbon composites for pantograph strip under electric current conditions. Tribol Int 2023;185:108483. https://doi.org/10.1016/j. triboint 2023.108483
- [23] Pang Y, Miao X, Zhang Q, Chen Z, Hao L, Zhong J, et al. Effect of graphene on the high-energy arc erosion performance of the W-Cu composite. Vacuum 2023;210: 111827. https://doi.org/10.1016/j.vacuum.2023.111827.
- [24] Dong L, Li L, Li X, Zhang W, Fu Y, Elmarakbi A, et al. Enhancing mechanisms of arc-erosion resistance for copper tungsten electrical contact using reduced graphene oxides in situ modified by copper nanoparticles. Int J Refract Met Hard Mater 2022;108:105934. https://doi.org/10.1016/j.ijrmhm.2022.105934.
 [25] Yin J, Zhang H, Xiong X, Tao H, Wang P, Deng C. Influence of applied load on wear
- [25] Yin J, Zhang H, Xiong X, Tao H, Wang P, Deng C. Influence of applied load on wear behavior of C/C-Cu composites under electric current. Progress Nat Sci Mater Int 2017;27:192–6. https://doi.org/10.1016/j.pnsc.2017.03.004.
- [26] Li A, Xie M, Yang Y, Zhang J, Wang S, Chen Y, et al. Effect of CNTs content on the mechanical and arc-erosion performance of Ag-CNTs composites. Diam Relat Mater 2022;128:109211. https://doi.org/10.1016/j.diamond.2022.109211.
- [27] Li A, Zhou W, Xie M, Wang S, Wang S, Yang Y, et al. Preparation and arc erosion behavior of AgNi10 contact material with different allotropes of carbon addition. Diam Relat Mater 2021;111:108141. https://doi.org/10.1016/j. diamond.2020.108141.
- [28] Alderete B, Schäfer C, Nayak UP, Mücklich F, Suarez S. Modifying the characteristics of the electrical arc generated during hot switching by reinforcing silver and copper matrices with carbon nanotubes. J Compos Sci 2024;8:285–304. https://doi.org/10.3390/jcs8070285.
- [29] Alderete B, Suarez S, Mücklich F. On the production & tribo-electrical characterization of carbon nanotube-reinforced ag & cu metal matrix composites. In: 2023 IEEE 68th Holm Conference on Electrical Contacts (HOLM). IEEE; 2023. p. 1–8. https://doi.org/10.1109/HOLM56075.2023.10352236.
- [30] Alderete B, Mücklich F, Suarez S. Electrical characterization of carbon nanotube reinforced silver and copper composites for switching contacts. J Compos Sci 2023; 7:284. https://doi.org/10.3390/jcs7070284.
- [31] Alderete B, Mücklich F, Suarez S. Evaluating the effect of unidirectional loading on the piezoresistive characteristics of carbon nanoparticles. Sci Rep 2024;14:9247. https://doi.org/10.1038/s41598-024-59673-5.
- [32] Suarez S, Alderete B, Puyol R, Mücklich F. Load-dependent electrical contact resistance of carbon nanotube-reinforced metal matrix composites. In: 2022 IEEE 67th Holm Conference on Electrical Contacts (HLM). IEEE; 2022. p. 1–6. https://doi.org/10.1109/HLM54538.2022.9969801.

- [33] Dresselhaus MS, Dresselhaus G, Saito R. Physics of carbon nanotubes. Carbon 1995;33:883–91. https://doi.org/10.1016/0008-6223(95)00017-8.
- [34] R. Saito, G. Dresselhaus, M.S. Dresselhaus, Physical Properties of Carbon Nanotubes, Published by Imperial College Press and Distributed by World Scientific Publishing Co., London, 1998. https://doi.org/10.1142/p080.
- [35] Hilding J, Grulke EA, George Zhang Z, Lockwood F. Dispersion of Carbon Nanotubes in Liquids. J Dispers Sci Technol 2003;24:1–41. https://doi.org/ 10.1081/DIS-120017941.
- [36] Robertson J, Zhong G, Hofmann S, Bayer BC, Esconjauregui CS, Telg H, et al. Use of carbon nanotubes for VLSI interconnects. Diam Relat Mater 2009;18:957–62. https://doi.org/10.1016/j.diamond.2009.02.008.
- [37] Puyol R, Suarez S. A contact resistance measurement setup for the study of novel contacts. In: 2017 IEEE URUCON. IEEE; 2017. p. 1–4. https://doi.org/10.1109/ URLICON.2017.8171881.
- [38] Suarez S, Puyol R, Schafer C, Mucklich F. Carbon nanotube-reinforced metal matrix composites as novel electrodes for low-voltage switching applications: a surface degradation analysis. In: 2019 IEEE Holm Conference on Electrical Contacts. IEEE; 2019. p. 135–41. https://doi.org/10.1109/HOLM.2019.8923921.
- [39] PDE Solutions Inc., FlexPDE, (2023). (https://www.pdesolutions.com/flexpde-7-s upport/) (accessed June 27, 2024).
- [40] Maly R. Spark Ignition: Its Physics and Effect on the Internal Combustion Engine. In: Fuel Economy. US, Boston, MA: Springer; 1984. p. 91–148. https://doi.org/ 10.1007/978-1-4899-2277-9 3.
- [41] Saggau B. Kalorimetrie der drei entladungsformen des elektrischen Zündfunkens. Arch FüR Elektro 1981;64:229–35. https://doi.org/10.1007/BF01574305.
- [42] Lowke JJ. Characteristics of Radiation-Dominated Electric Arcs. J Appl Phys 1970; 41:2588–600. https://doi.org/10.1063/1.1659268.
- [43] Soldera F, Lasagni A, Mücklich F, Kaiser T, Hrastnik K. Determination of the cathode erosion and temperature for the phases of high voltage discharges using FEM simulations. Comput Mater Sci 2005;32:123–39. https://doi.org/10.1016/j. compated 2004.06.004
- [44] Mills KC, Monaghan BJ, Keene BJ. Thermal conductivities of molten metals: part 1 Pure metals. Int Mater Rev 1996;41:209–42. https://doi.org/10.1179/ imr.1996.41.6.209.
- [45] Laubitz MJ. Transport properties of pure metals at high temperatures: I. copper. Can J Phys 1967;45:3677–96. https://doi.org/10.1139/p67-309.
- [46] Laubitz MJ. Transport properties of pure metals at high temperatures. II. Silver and gold. Can J Phys 1969;47:2633–44. https://doi.org/10.1139/p69-322.
- [47] Kirshenbaum AD, Cahill JA, Grosse AV. The density of liquid silver from its melting point to its normal boiling point 2450°K. J Inorg Nucl Chem 1962;24:333–6. https://doi.org/10.1016/0022-1902(62)80188-2.
- [48] Cahill JA, Kirshenbaum AD. The density of liquid copper from its melting point (1356°K) to 2500°K and an estimate of its critical constants. J Phys Chem 1962;66: 1080–2. https://doi.org/10.1021/i100812a027.
- [49] Chapman TW. The heat capacity of liquid metals. Mater Sci Eng 1966;1:65–9. https://doi.org/10.1016/0025-5416(66)90012-7.
- [50] Wang M, Pan N. Predictions of effective physical properties of complex multiphase materials. Mat Sci Eng R Rep 2008;63:1–30. https://doi.org/10.1016/j. mser 2008 07 001
- [51] T. Laetsch, R. Downs, Software for Identification and Refinement of Cell Parameters from Powder Diffraction Data of Minerals Using the RRUFF Project and American Mineralogist Crystal Structure Databases, in: Abstracts from the 19th General Meeting of the International Mineralogical Association, Kobe, Japan, 2006. (https://rruff.info/about/about_download.php) (accessed August 6, 2024).
- [52] MacLucas T, Grützmacher P, Husmann S, Schmauch J, Keskin S, Suarez S, et al. Degradation analysis of tribologically loaded carbon nanotubes and carbon onions. Npj Mater Degrad 2023;7. https://doi.org/10.1038/s41529-023-00346-5.

- [53] Ferrari AC, Robertson J. Interpretation of Raman spectra of disordered and amorphous carbon. Phys Rev B Condens Matter Mater Phys 1999;61:14095–107. https://doi.org/10.1103/PhysRevB.61.14095.
- [54] Chapman TW. The viscosity of liquid metals. AIChE J 1966;12:395–400. https://doi.org/10.1002/aic.690120233.
- [55] Gadelmawla ES, Koura MM, Maksoud TMA, Elewa IM, Soliman HH. Roughness parameters. J Mater Process Technol 2002;123:133–45. https://doi.org/10.1016/ S0924-0136(02)00060-2.
- [56] Abbott EJ, Firestone FA. Specifying surface quality a method based on accurate measurement and comparison. J Mech Eng 1933;55:569–72.
- [57] International Organization for Standardization (ISO), 13565 Geometrical Product Specifications (GPS) - Surface texture: Profile method; Surfaces having stratified functional properties, (1996).
- [58] Salcedo MC, Coral IB, Ochoa GV. Characterization of surface topography with Abbott Firestone curve. Contemp Eng Sci 2018;11:3397–407. https://doi.org/ 10.12988/ces.2018.87319
- [59] Alderete B, Nayak UP, Mücklich F, Suarez S. Influence of topography on electrical contact resistance of copper-based materials. Surf Topogr 2023;11:025027. https://doi.org/10.1088/2051-672x/acdfea.
- [60] Bigerelle M, Iost A. A numerical method to calculate the Abbott parameters: a wear application. Tribol Int 2007;40:1319–34. https://doi.org/10.1016/j. triboint.2006.12.007.
- [61] Laheurte R, Darnis P, Darbois N, Cahuc O, Neauport J. Subsurface damage distribution characterization of ground surfaces using Abbott–Firestone curves. Opt Express 2012;20:13551. https://doi.org/10.1364/OE.20.013551.
- [62] Reinert L, Zeiger M, Suárez S, Presser V, Mücklich F. Dispersion analysis of carbon nanotubes, carbon onions, and nanodiamonds for their application as reinforcement phase in nickel metal matrix composites. RSC Adv 2015;5: 95149–59. https://doi.org/10.1039/C5RA14310A.
- [63] Zhao X, Ando Y, Qin L-C, Kataura H, Maniwa Y, Saito R. Characteristic Raman spectra of multiwalled carbon nanotubes. Phys B Condens Matter 2002;323:265–6. https://doi.org/10.1016/S0921-4526(02)00986-9.
- [64] Zhao X, Ando Y, Qin L-C, Kataura H, Maniwa Y, Saito R. Multiple splitting of G-band modes from individual multiwalled carbon nanotubes. Appl Phys Lett 2002; 81:2550–2. https://doi.org/10.1063/1.1502196.
- [65] DiLeo RA, Landi BJ, Raffaelle RP. Purity assessment of multiwalled carbon nanotubes by Raman spectroscopy. /1–5 J Appl Phys 2007;101:064307. https:// doi.org/10.1063/1.2712152.
- [66] Suarez S, Lasserre F, Prat O, Mücklich F. Processing and interfacial reaction evaluation in MWCNT/Ni composites. Phys Status Solidi 2014;211:1555–61. https://doi.org/10.1002/pssa.201431018.
- [67] Maciejewska BM, Jasiurkowska-Delaporte M, Vasylenko AI, Koziot KK, Jurga S. Experimental and theoretical studies on the mechanism for chemical oxidation of multiwalled carbon nanotubes. RSC Adv 2014;4:28826–31. https://doi.org/ 10.1039/C4RA03881A.
- [68] RRUFF Project, Tenorite R120076 Raman Spectrum, (n.d.). (https://rruff.info/tenorite/names/asc/R120076) (accessed May 30, 2024).
- [69] RRUFF Project, Cuprite R140763 Raman Spectrum, (n.d.). (https://rruff.info/chem=Cu/chemistry/asc/display=default/R140763) (accessed May 30, 2024).
- [70] DiLeo RA, Landi BJ, Raffaelle RP. Application of the G'/D Raman ratio for purity assessment of multi-walled carbon nanotubes. MRS Proc 2011;1018. https://doi. org/10.1557/PROC-1018-EE05-11.
- [71] Lehman JH, Terrones M, Mansfield E, Hurst KE, Meunier V. Evaluating the characteristics of multiwall carbon nanotubes. Carbon 2011;49:2581–602. https:// doi.org/10.1016/j.carbon.2011.03.028.